ELSEVIER

Modeling transport and combustion of firebrands from burning trees

Nicolas Sardoy [a], Jean-Louis Consalvi [a], Bernard Porterie [a,*],
A. Carlos Fernandez-Pello [b]

[a] *IUSTI/UMR CNRS 6595, Technopôle de Château-Gombert, 5 Rue Enrico Fermi, 13453 Marseille cedex 13, France*
[b] *Department of Mechanical Engineering, University of California at Berkeley, Berkeley, CA 94720-1740, USA*

Abstract

Burning embers, commonly called firebrands, are lofted by a fire's buoyant plume and transported downwind to ignite new fires (spot fires) ahead of the main fire. In the present work, transport and combustion of firebrands from burning trees are numerically investigated. A three-dimensional physics-based model is used to precompute the steady-state gas flow and thermal fields induced by a crown fire into which firebrands will be injected. Another preliminary study of the thermal degradation and combustion of woody fuel particles is conducted to determine the burning characteristics of firebrands. Then the trajectories and burning rates of disk-shaped firebrands lofted by the crown fire plume and transported downwind are calculated for various values of the wind speed, U_{wind}, and of the fire intensity, I. Firebrands of different sizes and densities are first launched from a specified location at the top of the canopy. Firebrands that fall on the ground are in a flaming or a glowing state depending on the product $\rho_{\text{f}}^{\text{w0}} \times \tau$ ($\rho_{\text{f}}^{\text{w0}}$: initial firebrand density, τ: firebrand thickness). Results show that for firebrands that remain longer in the thermal plume, the distance covered upon landing is independent of the initial particle diameter and correlates well with $I^{0.1} U_{\text{wind}}^{0.9} (\rho_{\text{f}}^{\text{w0}} \times \tau)^{-0.2}$. The normalized brand mass fraction at landing also correlates with the flight time normalized by the product $\rho_{\text{f}}^{\text{w0}} \times \tau$ for flaming firebrands or by the product $\rho_{\text{f}}^{\text{w0}} \times D_0^{5/3}$ (D_0: initial firebrand diameter) for glowing firebrands. For firebrands released from random locations within the canopy, the above correlations remain unchanged, thereby demonstrating the generality of the developed approach.
© 2007 The Combustion Institute. Published by Elsevier Inc. All rights reserved.

Keywords: Spotting; Firebrand; Fire; Buoyant plume; Lofting; Burning embers

1. Introduction

The spotting process, whereby flaming or glowing embers, commonly called firebrands, are lofted by a fire plume and transported downwind to ignite new fires (spot fires) ahead of the main fire, is an important mechanism for wildland fire spread. Pieces of bark, needles, leaves, cones, twigs, and small branches are good candidates for spotting. Dense, short-distance spotting (up to tens of meters from the main fire front) may occur continuously, while occasionally, isolated spots or groups of spots may be ignited at longer distances (between hundreds of meters and a

---

* Corresponding author.
E-mail address: bernard.porterie@polytech.univ-mrs.fr
(B. Porterie).

Nomenclature

A	pre-exponential factor
A_k	specific wetted area of the solid phase, $\alpha_k \sigma_k$
c_p	specific heat
D	firebrand diameter
d	distance covered by the firebrands
f_{vs}	soot volume fraction
$\mathbf{g}$	gravity acceleration vector
G	average incident radiation, $G = \int_{4\pi} I(\boldsymbol{\Omega})\, d\Omega$
h	enthalpy
h_{conv}	heat transfer coefficient
Δh	heat of reaction
I	radiative intensity, fire intensity
I_b	black body radiative intensity ($I_b(T) = \sigma T^4 / \pi$)
k	turbulent energy
l	length of a cylinder-shaped firebrand
L	latent heat
M	firebrand mass
$\mathbf{n}$	unit vector normal to boundary ($\mathbf{n} = \mathbf{r}$ for cylinder-shaped brands, $\mathbf{n} = \mathbf{z}$ or $\mathbf{r}$ for disk-shaped brands)
Pr	Prandtl number
Q	energy influx
Sc	Schmidt number
T	temperature
U_{wind}	wind speed
v_f	volume of a firebrand
v_k	volume of a solid-phase (fuel bed) particle
$\mathbf{V}$	velocity vector
Y_α	mass fraction of species α

Greek symbols

α	phase volume fraction
α_i	incidence angle of disk-shaped firebrands
δ_{ij}	Kronecker delta
ε	dissipation rate of k, surface emissivity
λ	thermal conductivity
μ	viscosity
$\dot{\omega}_\alpha$	rate of production of species α
$\boldsymbol{\Omega}$	directional vector of radiative intensity
ρ	density
σ_k	surface-area-to-volume ratio of a solid-phase particle, $\sigma_k = s_k / v_k$
σ_ϕ	turbulent Prandtl/Schmidt number for ϕ
τ	thickness of a disk-shaped firebrand

Subscripts and superscripts

α	gas species ($\alpha = CO, O_2, CO_2, H_2O, N_2$)
char	residual char
f	firebrand
film	gas property calculated at the film temperature
final	firebrand property at landing
g	gas phase
k	solid phase (fuel bed)
n	time iteration level
ox	oxidation
pyr	pyrolysis
surf	firebrand surface
w	dry wood
0	initial value
∞	freestream value

few kilometers). There are many factors that affect spotting: the weather, topography, and fuel, which includes the receptive fuel bed propensity to ignite. Spotting is the dominant fire propagation mechanism in high-intensity forest fires (e.g., crown fires), with severe implications for prevention, forecasting, and combat. One may think of partial clearance of forest lands, house distribution in wildland–urban interface areas, and reduction in the firebreak efficiency. Prediction of spot fires and firebrand distribution requires understanding of the firebrand behavior, including their transport in convective plumes associated with different fire intensities and wind speeds, and their potential to ignite fuel beds on landing. The necessity of combining transport and combustion firebrand models with wildland fire convection plume

models is patently obvious. The present work focuses on the transport and combustion of firebrands, the ignition of the receptive fuel bed not being considered.

The transport and combustion of firebrands were first studied in the reference works of Tarifa et al. [1,2]. Laws of variation of radius and density for both spherical and cylindrical particles as functions of time, relative wind speed, kind of wood, and moisture content were deduced from wind tunnel experiments. Flight paths and lifetimes of burning wooden brands were then determined for both uniform ambient horizontal wind and basic vertical or inclined constant-velocity convection column models. The maximum distance reached by still-burning firebrands was estimated.

Lee and Hellman analytically modeled the aerodynamic behavior of spherical firebrands of constant density in a turbulent, swirling axisymmetric convection plume [3,4] and in Tarifa's two-dimensional tilted constant-velocity convection plume [4]. Using Tarifa's data for wood spheres, two empirical laws of the burning rate were established [3,4]. For the tilted convection plume, the flight paths of spherical firebrands were compared with those of Tarifa. The shapes of the trajectories obtained in both studies were similar, although those from Lee and Hellman were shorter in length.

Muraszew and Fedele [5] modeled two-dimensional trajectories of cylindrical firebrands released above a fire whirl. The firebrand combustion model required the time evolution of both density and diameter. From their experiments on firebrands generated in the fire whirl core, the authors obtained an exponential decay law of density. They also used Tarifa's relationship [2] to compute the diameter regression rate.

Albini developed a burning-rate model based on the linear relationship between two dimensionless groups: $x_{\text{Albini}} = (\rho_\infty U_{\text{wind}} t)/(\rho_f^w D)_0$ and $y_{\text{Albini}} = 1 - (\rho_f^w D)/(\rho_f^w D)_0$. The constant regression coefficient $K = 0.0064$ in the equation $y_{\text{Albini}} = K x_{\text{Albini}}$ was determined from the data of Muraszew et al. [6] for four wood species. From this firebrand combustion model, Albini derived a linear equation which describes the change in terminal velocity with time. He also modeled the two-dimensional trajectories of cylinder-shaped firebrands lofted by one or several torching trees [7] or a burning of heavy fuel accumulation [8] using a semiempirical model (based upon simplified submodels) to describe the structure of the steady flame and buoyant plume. From these results he determined the maximum height to which a firebrand is lofted as well as the maximum possible spot fire distance. He also considered the transport of firebrands by line thermals [9,10] for wind-driven fires. Thermals generated were assumed to provide the principal means of transporting particles. The maximum height of a lofted firebrand was found to be roughly proportional to the square root of thermal energy.

The work of Woycheese and Pagni [11] examined the lofting of spherical nonburning brands by a vertical Baum and McCaffrey plume. This work was extended to combusting spheres using a burning-droplet model (surface regression only, constant particle density) [12]. Brand lofting and propagation downwind were then approximated as separate processes by exposing spherical burning brands to a Baum and McCaffrey vertical plume in the lofting phase and a constant horizontal ambient wind during propagation [13]. Woycheese and Pagni [14] determined

the maximum propagation distance of combusting disk-shaped brands exposed to the above-mentioned two-distinct-component flow field. A stagnation-point combustion model was used and lift forces were considered in the propagation phase. A constant angle of attack, between the disk face and the relative wind, was assumed. The authors underlined that lift significantly enhances the spotting risk by increasing propagation distances. From an experimental point of view, studies [15,16] were conducted to complement the work of Tarifa [1,2] by providing data and a better understanding of the combustion of wooden brands of different geometrical shapes in forced flow.

Tse and Fernandez-Pello [17] developed a numerical model that allows the calculations of trajectories, thermal and mass histories, and lifetimes of thermally thin spherical metallic particles (burning or not burning) and burning embers, released at arbitrary heights in an ambient wind. This work was continued by Anthenien et al. [18], who assessed the potential of firebrands of various shapes (spheres, cylinders, and disks) to spread fires. The embers may be launched at a specific height or lofted by a buoyant Baum and McCaffrey fire plume and carried by an ambient wind using a firebrand combustion model that includes both in-depth pyrolysis and heterogeneous surface combustion.

Recently, Ellis [19] studied in detail the aerodynamic and combustion characteristics of the stringy bark firebrand samples (bark of *Eucalyptus obliqua*), such as the flaming time, burnout time, terminal velocity, and mass, thanks to experiments made in the CSIRO vertical wind tunnel. To determine the trajectories of samples, transport and combustion models were combined with a two-dimensional bushfire plume model [20]. The predictions of maximum spotting distance were determined for given fire intensity, wind speed, and initial height. The comparison with the 1962 Daylesford fire data showed that model results were in fairly good agreement with the experiments despite the lack of knowledge of some of the model parameters.

In this work a numerical model for the transport of burning brands lofted by the three-dimensional steady-state buoyant plume from a crown fire is presented. The plume is precomputed using a reduced version of a physics-based two-phase model [21,22]. The rates of biomass reduction due to thermal degradation are adjusted to give the desired crown fire intensity. It is expected that the physical presence of the vegetation cover will give relevant evaluations of the flow field and flame properties. Once the flow and thermal fields are obtained for the gas phase, firebrands are launched from the canopy of a group of burning trees. Disk-shaped firebrands are considered as they represent the highest potential risk for long-

range spotting [18]. A model for the pyrolysis and combustion of firebrands is also developed. Due to the lack of data on disk-shaped brands, this model is validated against experimental data for wooden cylinders placed in a constant-velocity wind field. Temperature and size histories and trajectories of firebrands are computed to estimate landing distances. Although this study focuses on crown fires, which are known to be excellent generators of embers for spotting, the same procedure could be applied to ground fires.

2. Transport of firebrands by a fire's buoyant plume

2.1. Fire model

A physics-based forest fire model, based on a two-phase description of the medium in which a gas flows through a multiclass fuel bed, has been developed [22]. The gas phase and each class of the solid phase (i.e., vegetation elements such as dead and living needles, leaves, and branches) in thermal nonequilibrium are assumed to be interdispersed and coupled by appropriate interaction terms. Each of them is treated as a continuum and governed individually by a set of time-dependent equations. In the present study, this model is reduced to calculate the steady three-dimensional buoyant plume representative of a wildland fire. This is achieved by assuming single-class thermally thin fuel particles with a constant temperature, and adjusting the rates of particle mass reduction relative to the thermal degradation of the solid to get prescribed fire intensities. Only the gas phase equations with source terms due to the solid-phase contribution need to be solved.

2.1.1. Governing equations for the gas phase

The gas flow is described by the Favre-averaged balance equations for mass, momentum, enthalpy, and species mass fraction. Turbulence is modeled using the RNG (renormalization group theory) k–ϵ closure with additional buoyancy-driven production/destruction. The general form of the elliptic differential equations is given by
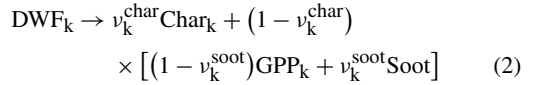
$$\frac{\partial}{\partial t}(\rho\phi) + \frac{\partial}{\partial x_j}(\rho\phi u_j) = \frac{\partial}{\partial x_j}\left(\Gamma_\phi \frac{\partial\phi}{\partial x_j}\right) + S_\phi. \quad (1)$$

In Table 1, the source terms, S_Φ, and the effective exchange coefficients, Γ_Φ, are summarized for the different variables and the constants of the turbulence model are listed.
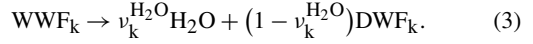
2.1.2. Chemical model

Thermal degradation of wet wildland fuel matter (WWF$_k$) is a two-step mechanism where the en-

dothermic pyrolysis reaction

$$\mathrm{DWF_k} \rightarrow \nu_k^{\mathrm{char}}\mathrm{Char_k} + \left(1 - \nu_k^{\mathrm{char}}\right) \\ \times \left[\left(1 - \nu_k^{\mathrm{soot}}\right)\mathrm{GPP_k} + \nu_k^{\mathrm{soot}}\mathrm{Soot}\right] \quad (2)$$

is preceded by the endothermic drying reaction

$$\mathrm{WWF_k} \rightarrow \nu_k^{\mathrm{H_2O}}\mathrm{H_2O} + \left(1 - \nu_k^{\mathrm{H_2O}}\right)\mathrm{DWF_k}. \quad (3)$$

DWF$_k$ and GPP$_k$ symbolize dry wildland fuel matter and gaseous pyrolysis products, respectively. For various forest fuels, the composition of pyrolysis products is complicated (CO, CO_2, CH_4, H_2, C_2H_6, etc.) and temperature-dependent. For simplicity, since the carbon monoxide is the most abundant component among the gaseous combustible products, it is taken as the combustible gas [26]. In the present study, $\mathrm{GPP_k} = \alpha_k^{\mathrm{CO}}\mathrm{CO} + (1 - \alpha_k^{\mathrm{CO}})CO_2$, where α_k^{CO} is the combustible part of GPP$_k$. The major gas species which are taken into consideration are then CO, O_2, CO_2, H_2O, and N_2. Moreover, Grishin [26] showed that a more representative seven-component combustible mixture (adding CH_4 and H_2 to the five-component mixture) led to no more than a 4% temperature deviation.

The source terms that appear in the gas phase equations (see Table 1) as a consequence of thermal degradation of the fuel material are deduced from the rates of water vaporization, $R_k^{\mathrm{H_2O}}$, and pyrolysis, R_k^{pyr}:

$$S_{Y_\alpha} = \begin{cases} (1 - \nu_k^{\mathrm{char}})(1 - \nu_k^{\mathrm{soot}})\alpha_k^{\mathrm{CO}}R_k^{\mathrm{pyr}}, \\ 0, \\ (1 - \nu_k^{\mathrm{char}})(1 - \nu_k^{\mathrm{soot}})(1 - \alpha_k^{\mathrm{CO}})R_k^{\mathrm{pyr}}, \\ R_k^{\mathrm{H_2O}}, \\ 0. \end{cases} \quad (4)$$

The pyrolysis rate is adjusted to obtain the desired fire intensity. Concerning the chemical reactions in the gas phase, use is made of a single-step CO oxidation reaction: $CO + \frac{1}{2}O_2 \rightarrow CO_2$.

Assuming fast oxidation, the burning rate of carbon monoxide is limited by the turbulence dissipation rates of either fuel, oxygen, or hot products, the slowest of which will control the local reaction rate [27]. Thus, the mass rate of production of gaseous species due to the above reaction can be determined from

$$\dot{\omega}_{\mathrm{CO}} = -\rho\frac{\epsilon}{k}\min\left(C_R Y_{\mathrm{CO}}, C_R\frac{Y_{\mathrm{O_2}}}{s_1}, \frac{C_R' Y_{\mathrm{CO_2}}}{1 + s_1}\right),$$

$$\dot{\omega}_{\mathrm{O_2}} = s_1\dot{\omega}_{\mathrm{CO}}, \quad \text{and} \quad \dot{\omega}_{\mathrm{CO_2}} = -(1 + s_1)\dot{\omega}_{\mathrm{CO}}, \quad (5)$$

where C_R and C_R' are constants taken to be 4 and 2, respectively, and s_1 the stoichiometric ratio of the chemical reaction ($s_1 = 4/7$).

Table 1
Summary of the key equations expressed in the generic form

Transport of	ϕ	Γ_ϕ	S_ϕ
Mass	1	0	$\sum_{\alpha=1}^{5} S_{Y_\alpha}$
Momentum	u_i	μ_{eff}	$-\alpha_g \dfrac{\partial p_g}{\partial x_i} + \rho g_i - \dfrac{2}{3}\dfrac{\partial}{\partial x_j}\left[\left(\mu_{\text{eff}}\dfrac{\partial u_k}{\partial x_k} - \rho k\right)\delta_{ij}\right]$ $+ \dfrac{\partial}{\partial x_j}\left(\mu_{\text{eff}}\dfrac{\partial u_j}{\partial x_i}\right) - [F_i]_k$
Enthalpy	h	$\dfrac{\mu}{\text{Pr}} + \dfrac{\mu_t}{\sigma_t}$	$-Q_{g,\text{radiative}} - Q_{k,\text{convective}} + \sum_{\alpha=1}^{5} S_{Y_\alpha} h_\alpha$
Kinetic energy of turbulence	k	$\mu + \dfrac{\mu_t}{\sigma_k}$	$P + W - \rho\varepsilon$
Rate of dissipation of turbulent energy	ε	$\mu + \dfrac{\mu_t}{\sigma_\varepsilon}$	$(C_{\varepsilon 1} - R)\dfrac{\varepsilon}{k}P - C_{\varepsilon 2}\rho\dfrac{\varepsilon^2}{k} + C_{\varepsilon 3}\dfrac{\varepsilon}{k}W$
Soot volume fraction	f_{vs}	$\dfrac{\mu_t}{\sigma_f}$	$-\dfrac{\partial}{\partial x_j}\left(\dfrac{0.55\mu}{T}\dfrac{\partial T}{\partial x_j}f_{vs}\right) + \dfrac{\rho\nu_k^{\text{soot}}R_k^{\text{pyr}}}{\rho_{\text{soot}}}\left(1 - \nu_k^{\text{char}}\right)$
Species mass fraction	Y_α	$\dfrac{\mu}{\text{Sc}} + \dfrac{\mu_t}{\sigma_f}$	$\dot\omega_\alpha + S_{Y_\alpha}$

Note. ϕ is the generic fluid property, Γ_ϕ and S_ϕ the exchange coefficient and source/sink terms for ϕ, where $\rho = \alpha_g\rho_g$, $\mu = \alpha_g\mu_g$, $\mu_t = \rho C_\mu k^2/\varepsilon$, $\mu_{\text{eff}} = \mu + \mu_t$, and ρ_{soot} is the soot density, assumed to be 1800 kg m^{-3}. In the enthalpy equation, the species enthalpy is determined at the temperature of the solid-phase surface: $h_\alpha = h_\alpha(T_k)$. The shear and buoyancy turbulence production/destruction terms P and W can be expressed by

$$P = \left[\mu_t\left(\frac{\partial u_i}{\partial x_j} + \frac{\partial u_j}{\partial x_i}\right) - \frac{2}{3}\left(\mu_t\frac{\partial u_k}{\partial x_k} + \rho k\right)\delta_{ij}\right]\frac{\partial u_i}{\partial x_j}, \qquad W = g\frac{\mu_t}{T\sigma_t}\frac{\partial T}{\partial x_j},$$

with

$$R = \frac{\eta(1 - \eta/\eta_0)}{1 + \beta\eta^3}, \quad \eta = \sqrt{\left|\frac{P}{\rho C_\mu\varepsilon}\right|},$$

$\eta_0 = 4.38$, $\quad \beta = 0.015$, $\quad C_\mu = 0.0845$, $\quad C_{\varepsilon 1} = 1.42$, $\quad C_{\varepsilon 2} = 1.68$, $\quad C_{\varepsilon 3} = 1.5$, $\quad \sigma_k = 0.7179$,

$\sigma_\varepsilon = 1.3$, $\quad \sigma_f = \sigma_t = 0.7$, $\quad \text{Sc} = \text{Pr} = 0.71$.

The gas is assumed to be a mixture of perfect gases

$$p_g = \rho_g RT\sum_\alpha \frac{Y_\alpha}{W_\alpha}.$$

The static enthalpy of the mixture is defined to include the chemical energy

$$h = \sum_\alpha Y_\alpha\left[\Delta h_{f\alpha}^0 + \int_0^T C_{p\alpha}(T)\,dT\right].$$

For each of the chemical species, polynomial expressions are used for the calculation of the specific heats, as a function of temperature, and of the standard heat of formation at 0 K (CHEMKIN data base, [23]). The drag force per unit volume acting on the solid-phase particles $[F_i]_k$, which appears in the gas phase momentum equation, can be calculated from the correlation proposed by [24] for cylinders. As the two phases are not in local thermal equilibrium, an interfacial convective heat transfer is used to take the interaction between them into account, $Q_{k,\text{convective}} = A_k h_k(T - T_k)$, where the heat transfer coefficient is expressed from the correlation of [25].

2.1.3. Radiation transport and soot formation

The divergence of the radiative heat flux, $\mathbf{q}_r$, which appears in the energy equation of the gas phase can be expressed as

$$Q_{g,\text{radiative}} = -\nabla.\mathbf{q}_r = \alpha_g a_g\big[G - 4\pi I_b(T)\big]. \qquad (6)$$

For an absorbing–emitting gray particulate medium, a multiphase radiative transfer equation (MRTE) has been developed in [28]. For a single-class solid phase, the radiative intensity in the direction $\boldsymbol{\Omega}$, $I(\boldsymbol{\Omega})$, obeys the following equation:

$$\Omega_j\frac{\partial}{\partial x_j}(\alpha_g I) + (\alpha_g a_g + \alpha_k a_k)I$$
$$= \alpha_g a_g I_b(T) + \alpha_k a_k I_b(T_k). \qquad (7)$$

The absorption coefficient a_k for the solid phase can be calculated from $a_k = A_k/4$ [28], while that of the soot/combustion products (CO_2, H_2O) mixture considered as a gray gas is evaluated from the mole fraction of the combustion products and the soot volume fraction [29]: $a_g = 0.1(X_{CO_2} + X_{H_2O}) + 1862 f_{vs}T$.

As incandescent soot particles are the main contributors to overhead flame radiation, an accurate prediction of radiative transfer requires accounting for soot formation, especially in turbulent flames. In the present soot model, only one equation is used, namely a transport equation for the volume fraction of soot f_{vs}. The source terms in the soot transport equation (see Table 1) account for thermophoresis and formation processes. In accordance with Grishin [26], we can assume that most of the soot in the flame is produced as a result of the pyrolysis of wildland fuels. The rate of soot formation is then proportional to that of pyrolysis [22].

2.1.4. Solution procedure

The conservation equations (Eq. (1), Table 1) are discretized on a staggered, nonuniform Cartesian three-dimensional grid using a finite-volume procedure with a second-order backward Euler scheme for time integration. Diffusion terms are approximated using a second-order central difference scheme. The ULTRASHARP approach, which combines the use of a high-order upwind scheme for the convective terms and of a flux limiter strategy [30] is used. The pressure–velocity linked equations are solved using the iterative PISO algorithm developed by Chow and Cheung [31]. The resulting systems of linear algebraic equations for each variable are then solved iteratively using the line-by-line tridiagonal matrix algorithm (TDMA) [32]. In order to accelerate convergence, all the gas variables are underrelaxed using inertial relaxation. The solution of the radiative transfer equation is obtained from the finite-volume method of Raithby and Chui [33].

2.2. Firebrands momentum equations

Trajectories of disk-shaped firebrands are computed from Newton's second law of motion. Position and velocity are calculated for each firebrand by solving the initial-value problem

$$\frac{d\mathbf{r}_f}{dt} = \mathbf{V}_f, \tag{8}$$

$$\rho_f v_f \frac{d\mathbf{V}_f}{dt} = v_f(\rho_f - \rho_{film})\mathbf{g} + \mathbf{F}_D + \mathbf{F}_L. \tag{9}$$

The subscript film indicates that the associated gas property is taken at the film temperature, which is the average between the gas and the particle surface temperature.

The drag and lift forces, $\mathbf{F}_D$ and $\mathbf{F}_L$, are expressed as

$$\mathbf{F}_D = \frac{1}{2}C_D \rho_{film} S_{eff1} \|\mathbf{V}_{rel}\| \mathbf{V}_{rel}, \tag{10}$$

$$\mathbf{F}_L = \frac{1}{2}C_L \rho_{film} S_{eff2} \frac{\mathbf{y}' \cdot \mathbf{V}_{rel}}{\|\mathbf{V}_{rel}\|}[\mathbf{y}' \times \mathbf{V}_{rel}] \times \mathbf{V}_{rel}. \tag{11}$$

S_{eff1} and S_{eff2} are the respective particle areas normal to the direction of the drag and lift forces. They depend on the incidence angle (α_i) between the relative velocity $\mathbf{V}_{rel}$ and firebrand major axis direction ($\mathbf{y}'$) assumed to be lied in the plane (xy), and are determined from [34]

$$S_{eff1} = \frac{\pi D^2}{4}\left[\sin^2\alpha_i + \left(\frac{4}{\pi}AR\right)^2\cos^2\alpha_i\right]^{1/2}, \tag{12}$$

$$S_{eff2} = \frac{\pi D^2}{4}\left[\cos^2\alpha_i + \left(\frac{4}{\pi}AR\right)^2\sin^2\alpha_i\right]^{1/2}, \tag{13}$$

where AR ($= \tau/D$) is the aspect ratio of the disk-shaped particle.

The lift and drag coefficients finally are defined as

$$C_D = C_N \sin\alpha_i - C_T \cos\alpha_i, \tag{14}$$

$$C_L = -C_N \cos\alpha_i - C_T \sin\alpha_i, \tag{15}$$

where the normal force coefficient C_N and the tangential force coefficient C_T [35] are given by

$$C_N = \frac{C_D(90)\sin\alpha_i}{0.56 + 0.44\sin\alpha_i}, \tag{16}$$

$$C_T = -1/2 \cdot 0.0075\cos\alpha_i. \tag{17}$$

The two-dimensional drag coefficient for an angle of attack of 90°, $C_D(90)$, is given as a function of aspect ratio and it is fitted by [35]

$$C_D(90) = 1.98 - 0.81\big(1 - \exp(-20/AR)\big). \tag{18}$$

2.3. Thermal degradation and combustion of firebrands

A critical component in the theoretical prediction of the firebrands' trajectories is the modeling of their thermal degradation and combustion. A study of this problem is presented below. Since there is no experimental data for disk-shaped particles, cylinders are also considered for the validation of the model performed in this subsection.

2.3.1. Model description

A schematic representation of the cylinder-shaped and disk-shaped dry woody fuel particles studied here is shown in Fig. 1. The model is based on the following assumptions:
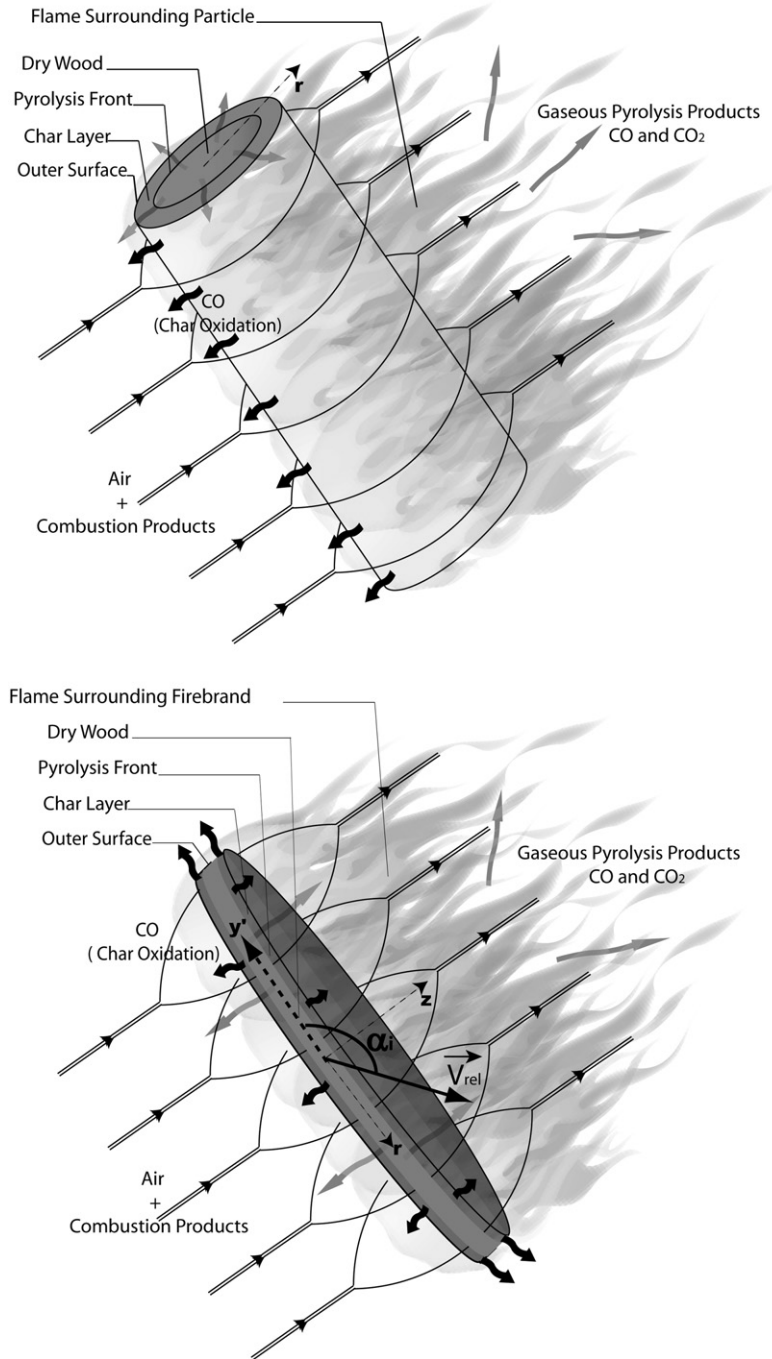
Fig. 1. Schematic representation of a cylinder-shaped and a disk-shaped dry wood particle undergoing pyrolysis and char oxidation.

(1) As the particle undergoes thermal degradation and combustion processes, it loses mass and volume. Pyrolysis is a subsurface volumetric chemical process whereas heterogeneous combustion (char oxidation) occurs at the outer surface of the particle. Consequently, the particle loses mass via in-depth pyrolysis and heterogeneous combustion; and it loses volume only from the heterogeneous combustion [17].

(2) Pyrolysis kinetics is modeled by a single-step first-order reaction leading to the formation of volatiles and char.

(3) In agreement with Grishin [26], the gaseous pyrolysis products (GPP_f) are an effective gas mixture of CO and CO_2. This leads to $GPP_f = \alpha_f^{CO}CO + (1 - \alpha_f^{CO})CO_2$, where α_f^{CO} is the combustible part of GPP_f.

(4) Heat and mass transfers are one-dimensional. Pyrolysis front moves through the particle along the diameter for cylinder-shaped brands while it moves along the thickness for disks. Concerning the char oxidation, the particle loses volume only by diameter regression. Observations of burning firebrands with small aspect ratio suggest that they smolder from the edge inward, rather than over the entire face through the thickness of the brand [18].

(5) Gaseous pyrolysis products leave the solid as soon as they are produced. They are in thermal equilibrium with the solid matrix.

(6) During the pyrolysis process, following Tse and Fernandez-Pello [17], the particle surface temperature remains constant and equal to 993 K.

(7) Char consists of pure carbon. Its oxidation is a one-step kinetic model which considers only the primary oxidation of all carbon atoms into CO. This process is controlled by oxygen diffusion at the outer surface particle.

(8) During pyrolysis, the supply of oxygen is limited by the release of volatiles and by the presence of the flame around the particle. Due to wake effects, oxygen can reach some regions of the particle where char oxidation can occur. At the end of pyrolysis, only char oxidation at the surface takes place.

(9) Firebrands are idealized as disks or cylinders. They hold their shape while burning.

The firebrand degradation process can be summarized by the following simplified mechanism:

- Endothermic global pyrolysis reaction

$$DWF_f \rightarrow \nu_f^{char}Char + (1 - \nu_f^{char}) \times \left[(1 - \nu_f^{soot})GPP_f + \nu_f^{soot}Soot\right], \tag{19}$$
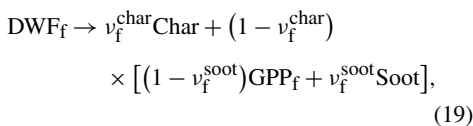
where DWF_f symbolizes dry fuel matter of firebrands.

- Exothermic one-step char oxidation reaction which considers primary oxidation of all carbon atoms into carbon monoxide: $C + \frac{1}{2}O_2 \rightarrow CO$.

Under the previous assumptions, the governing conservation equations for both the solid matrix and the gaseous products can be written as follows:

- Wood mass balance:

$$\frac{\partial \rho_f^w}{\partial t} = -R_f^{pyr}. \tag{20}$$

- Char mass balance:

$$\frac{\partial \rho_f^{char}}{\partial t} = \nu_f^{char}R_f^{pyr}, \tag{21}$$

where the rate of mass loss due to in-depth pyrolysis is expressed by

$$R_f^{pyr} = \rho_f^w A_f^{pyr} \exp\left(\frac{-T_f^{pyr}}{T_f}\right). \tag{22}$$

In this equation T_f^{pyr} is the activation temperature of pyrolysis.

During char oxidation, it is assumed that the particle undergoes volume loss while its density remains constant. So the rate of volume loss due to heterogeneous combustion is described by the equation

$$\rho_f^{char}\frac{\partial v_f}{\partial t} = -R_f^{char}S_{ox}, \tag{23}$$

where S_{ox} is the outer surface, which undergoes char oxidation.

For the cylinder-shaped brands, $S_{ox} = \pi Dl/2$ or πDl for pyrolysis or char oxidation process, respectively. For disks, l is replaced with τ.

If the relative velocity of air with respect to the particle is zero, the rate of reaction R'_{char} can be expressed by [36]

$$R_f'^{char} = -\frac{48}{32}\left(\frac{D_{iff_0}}{D}\right)\rho_0\left(\frac{T_{film}}{273}\right)^{0.75} \times \frac{1}{\gamma}\ln(1 - \gamma Y_{O_2 surf}), \tag{24}$$

where $D_{iff_0} = 18 \times 10^{-6}$ $m^2\,s^{-1}$ and ρ_0 are the oxygen diffusion coefficient and gas density at 273 K. The Stefan coefficient, γ, takes into account only the primary oxidation in contact with carbonaceous surface. For a one-step char oxidation reaction, $\gamma = -1$. $Y_{O_2 surf}$ is the mass fraction of O_2 transported from the gas to the particle surface by diffusion.

When there is a relative motion between the air flow and the particle, the global reaction rate R_{char} can then be expressed from R'_{char} as [37]

$$R_f^{char} = R_f'^{char}[1 + 0.272Sc^{1/3}Re^{1/2}], \tag{25}$$

where $Re = D_{sphere}\rho_{film}\|V_{rel}\|/\mu_{film}$ is the Reynolds number based on the relative velocity between the particle and the surrounding gas, V_{rel}, and the equal-volume sphere diameter D_{sphere}.

- Conservation of mass flux of gaseous fuel species:

$$\nabla \cdot \left(\dot{m}''_{CO} \mathbf{n} \right) = \left(1 - \nu_f^{char}\right) \alpha_f^{CO} R_f^{pyr} \left(1 - \nu_f^{soot}\right), \tag{26}$$

$$\nabla \cdot \left(\dot{m}''_{CO_2} \mathbf{n} \right) = \left(1 - \nu_f^{char}\right)\left(1 - \alpha_f^{CO}\right) \\ \times R_f^{pyr} \left(1 - \nu_f^{soot}\right). \tag{27}$$

- Energy balance:

$$\left(\rho_f^w c_p^w + \rho_f^{char} c_p^{char} \right) \frac{\partial T_f}{\partial t} + \dot{m}''_g c_{p_g} \mathbf{n} \cdot \nabla T_f \\ = \nabla \cdot \left(\lambda_f \nabla T_f \right) - R_f^{pyr} L_f^{pyr}, \tag{28}$$

where $\dot{m}''_g c_{p_g} = \dot{m}''_{CO} c_{p_{CO}} + \dot{m}''_{CO_2} c_{p_{CO_2}}$.

The thermal conductivity λ_f is assumed to vary with the composition of the solid fuel according to $\lambda_f = \eta_f \lambda_f^w + (1 - \eta_f) \lambda_f^{char}$, where $\eta_f = \rho_f^w / \rho_f^{w0}$.

Initial and boundary conditions are needed to close the system of equations. Initially, the temperature inside the particle is uniform and equal to the initial gas temperature. Along the axis of the particle, the symmetry condition is applied. At the surface of the particle, during pyrolysis, temperature is assumed to be constant and equal to 993 K. Upon pyrolysis, the surface temperature is deduced from the surface energy balance including convective and radiative losses as well as the chemical feedback due to char oxidation:

$$-\lambda_f (\nabla T_f \cdot \mathbf{n})_{surf} \\ = h_{conv} \left(T_f^{surf} - T_{film} \right) + \varepsilon_f \left(\sigma T_f^{surf4} - \frac{G}{4} \right) \\ + \alpha_f^{char} R_f^{char} \Delta h_f^{char}. \tag{29}$$

α_f^{char} is the fraction of energy released by the char oxidation that is deposited in the particle.

The heat transfer coefficient, h_{conv}, is calculated through the Nusselt number $Nu = h_{conv} D / \lambda_{film}$ given by the correlation of Kramers [25] as cited in [18]

$$Nu = 0.42 Pr^{0.2} + 0.57 Re^{1/2} Pr^{1/3}$$

(valid for $1 < Re < 10^4$). $\tag{30}$

The system of equations is solved by a finite volume method. When char oxidation occurs, an adaptive remesh procedure is performed as the particle surface regresses.

2.3.2. Validation with experiments

Experimental data from the Northern Forest Fire Laboratory (1975) on dry limbwood samples including bark, reported by Muraszew et al. [6], are used for comparisons. Several species of trees are considered: Ponderosa pine (PP), Engelmann spruce (ES),

Table 2
Firebrand properties and thermokinetic constants

Property	Value	Units	References
ε_f	0.9	–	[38]
ν_f^{char}	0.39 (Ponderosa pine)	–	[26]
	0.33 (others species of trees)	–	[26]
ν_f^{soot}	0.03	–	[26]
λ_f^w	0.24	$W\,m^{-1}\,K^{-1}$	[39]
λ_f^{char}	0.1	$W\,m^{-1}\,K^{-1}$	[39]
c_{pf}^w	1466	$J\,kg^{-1}\,K^{-1}$	[39]
c_{pf}^{char}	1100	$J\,kg^{-1}\,K^{-1}$	[39]
α_f^{CO}	0.80	–	[26]
α_f^{char}	0.33	–	[26]
L_f^{pyr}	418	$kJ\,kg^{-1}$	[26]
Δh_f^{char}	-12×10^3	$kJ\,kg^{-1}$	[26]
A_f^{pyr}	725 (Ponderosa pine)	s^{-1}	[26]
	3.2 (others species of trees)	s^{-1}	[26]
T_f^{pyr}	6899 (Ponderosa pine)	K	[26]
	4402 (others species of trees)	K	[26]

western larch (WL), and western red cedar (WRC). These experiments consider the combustion of cylinders with different initial sizes and masses, each initially 10.2 cm long (5 in long in [6]). For each species of trees, two constant wind velocities are used: 4.47 and 6.71 m s^{-1} (10 and 15 mph in [6]).

Fuel properties and thermokinetic constants are summarized in Table 2 for the species of trees considered. All gas properties at the film temperature are computed using the CHEMKIN database [23]. The experimental data from 33 tests over fixed periods of burning on ovendried limbwood sections are reported in Fig. 2 in terms of Albini's analysis parameters x_{Albini} and y_{Albini} (see Introduction). Albini fitted these experimental data to determine the regression coefficient (K in $y_{Albini} = K x_{Albini}$) for the four species considered. That allowed him to establish a firebrand burning rate model [7]. The average incident radiation is defined from the ambient temperature as $G = 4\sigma T_0^4$. Model results are shown in Fig. 2 and compared with experimental data. A fairly good agreement is obtained with a maximum deviation of 28%. A 17% maximum mean deviation is obtained for WRC samples, whereas it is about 14% for ES firebrands, and no more than (8%) for WL and PP samples. By comparing the linear fit of model results ($K = 0.0061$) with that of experimental data ($K = 0.0064$), it is found that the model slightly underestimates the fractional loss of (density × diameter). The discrepancies between model and experiments
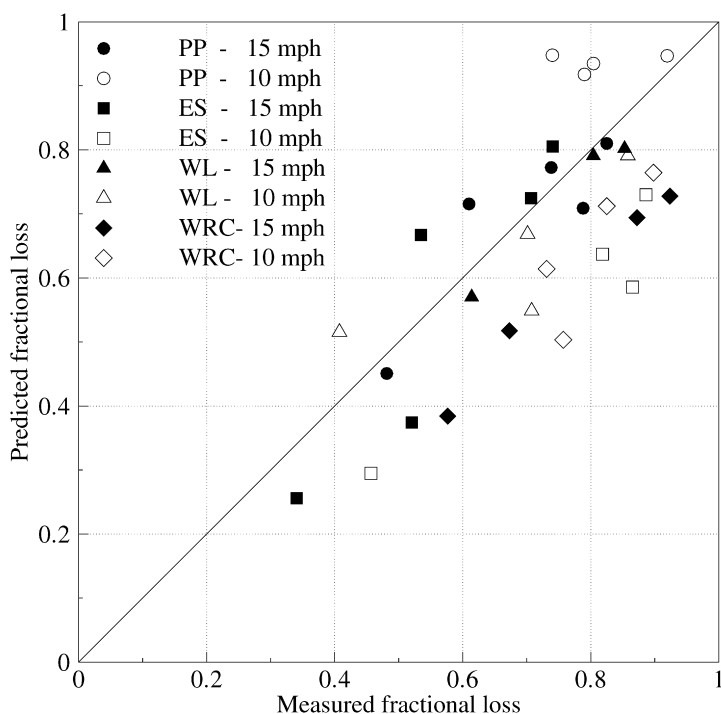
Fig. 2. Predicted versus measured [6] fractional loss of the product $\rho_f^w \times D$.

can be attributed mainly to the difficulty in determining thermokinetic constants.

3. Results and discussions

3.1. Computational details

The computational domain is 1000 m long, 400 m high, and 500 m wide. The burning fuel occupies a volume of $5 \times 5 \times 10$ m ($I = 10\,\mathrm{MW\,m}^{-1}$) or $5 \times 20 \times 10$ m ($I = 40\,\mathrm{MW\,m}^{-1}$) as an idealized representation of the canopy of a group of 8- or 23-m-high trees (Fig. 3). Considering preliminary results of Section 2, a live Ponderosa pine needle bed is used as a test fuel bed, whereas firebrands are limbs of the same tree species. The crown base height is located 3 m above the ground level. Since this problem is symmetric with respect to the central plane of the domain in the wind direction, only half of the domain is considered. A grid-independent solution is obtained using a grid density of $105 \times 80 \times 20$ with a refined mesh of $40 \times 38 \times 5$ cells of constant size in the fuel bed. The time step is 0.025 s. The steady-state solution of the Favre-averaged Navier–Stokes equations is reached when the relative convergence criterion $|\phi^{n+1} - \phi^n|/|\phi^n| \leqslant 10^{-4}$ is satisfied everywhere in the calculation domain. At least 8000 time iterations are needed to provide steady-state flow and thermal

fields. A typical run takes about 100 h of CPU time on a 3-GHz Pentium D processor and requires 1.5 GB of RAM.

The relative humidity is assumed to be constant and equal to 40%. At the upstream boundary, the incoming air flow is taken as that corresponding to the atmospheric surface layer with a uniform flat terrain. Assuming neutral stratification of the atmosphere, air flow properties depend on height, y, surface roughness, y_0, turbulent friction velocity, u^*, and Monin–Obukhov length according to [40]

$$u_x = 2.5u^* \ln(y/y_0), \qquad k = u^{*2}/\sqrt{C_\mu},$$
$$\varepsilon = 2.5u^{*3}/y \quad \text{with } u^* = \frac{U_{\mathrm{wind}}}{2.5\ln(H/y_0)} \tag{31}$$

and $y_0 = 3.8 \times 10^{-5}$ m. In this equation, U_{wind} is the known mean wind speed at a given height, H, and u_x is the desired wind speed at any other height, y. Wind speeds of 4.4, 6.7, and 8.9 m s^{-1} (10, 15, and 20 mph) at a height of 10 m are considered.

Initial and boundary conditions are summarized in Table 3.

The rate of fuel pyrolysis, R_k^{pyr}, is adjusted to obtain the desired release rate P (W m^{-1}) $= R_k^{\mathrm{pyr}} V \Delta h_f / z_c$, where V (m^3), z_c (m), and Δh_k (J kg^{-1}) are the volume occupied by the tree crown, its width, and the heat of reaction of the fuel, respectively. This can be compared with the fire in-
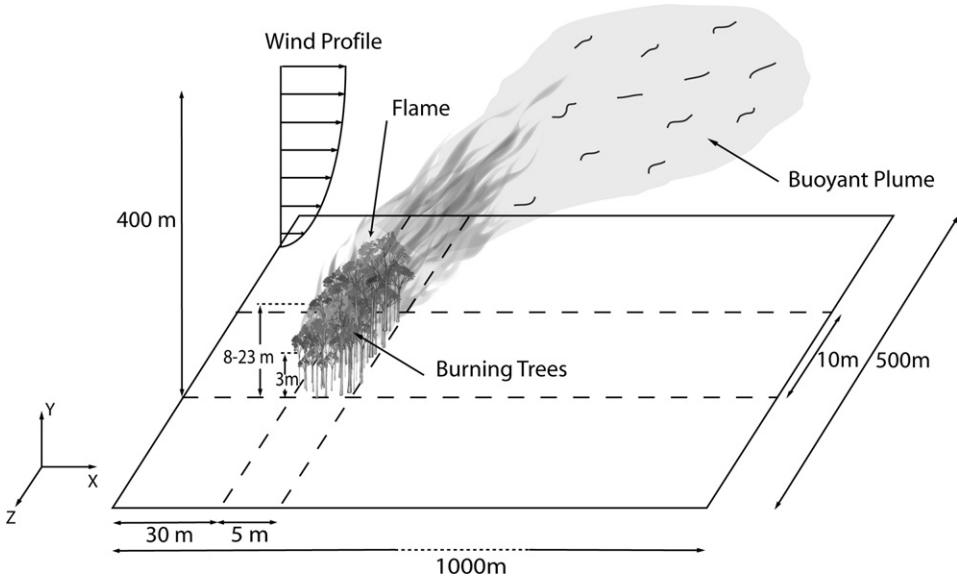
Fig. 3. Schematic of the physical problem, computational domain, and coordinate system used in the analysis.

Table 3
Initial and boundary conditions for the gas phase

	Initial conditions
	$\mathbf{u}_0 = \mathbf{0}$, $T_0 = 300$ K, $f_{vs_0} = 0$, $\varepsilon_0 = 10^{-6}$ m^2 s^{-3}, $k_0 = 10^{-6}$ m^2 s^{-2} $Y_{\alpha_0} = (0;\ 0.231;\ 0;\ 0.006;\ 0.763)$ $p_0 = p_\infty \exp\left(-gy/RT_0 \sum_\alpha \frac{Y_{\alpha_0}}{W_\alpha}\right)$ with $p_\infty = 101{,}325$ Pa ρ_0 and h_0 are deduced from the equations of state (see Table 1). $\alpha_g = \begin{cases} 1 & \text{outside the vegetation} \\ 1 - \alpha_k & \text{inside the vegetation} \end{cases}$
	Boundary conditions
Ground	$\mathbf{u} = \mathbf{0}$ $\frac{\partial \phi}{\partial n} = 0$ for $\phi = h$, f_{vs}, Y_α $k = 0$ $\varepsilon_p = \frac{C_\mu^{0.75} k_p^{1.5}}{\kappa \Delta_p}$, where p is the index of the first calculation point at a height Δ_p above the ground, and κ is the Von Karmann constant
Symmetry plane	$u_z = 0$, $\frac{\partial \phi}{\partial z} = 0$ for $\phi \neq u_z$
Outflow	$p = p_0$, $\frac{\partial \phi}{\partial n} = 0$ for $\phi \neq p$
Inflow	$\frac{\partial p}{\partial n} = 0$, $u_y = u_z = 0$, $Y_\alpha = Y_{\alpha_0}$, $f_{vs} = 0$, $T = T_0$, $h = h_0$ u_x, k, and ε are given by Eq. (31)

Table 4
Solid phase properties (Ponderosa pine needles) used in the fire model

Property	Value	Units
$R_k^{H_2O}$	0.0025	kg m^{-3} s^{-1}
R_k^{pyr}	0.020	kg m^{-3} s^{-1}
ν_k^{soot}	0.03	–
ν_k^{char}	0.3	–
α_k^{CO}	1.	–
Temperature T_k	1200	K
Surface-area-to-volume ratio σ_k	5000	m^{-1}
Volume fraction α_k	2.44×10^{-3}	–

Byram's equation [41]: I (W m^{-1}) $= wr\,\Delta h_k$, where w (kg m^{-2}) is the unit area fuel consumption and r (m s^{-1}) is the rate of spread. Data used for 10 and 40 MW m^{-1} fires, typical of Mediterranean crown fires, are given in Table 4.

Preliminary calculations of the buoyant plume above a steady-state forest fire are carried out to determine the local properties of the gas surrounding each firebrand during its flight. Once the fire thermal plume is fully determined, the trajectories and thermal behavior of the firebrands which are dragged out of canopy can be calculated. Particles are launched from the same position, i.e., at the ridge between the top side ($y_0 = 8$ m for $I = 10$ MW m^{-1} and $y_0 = 23$ m for $I = 40$ MW m^{-1}) and the leeward side of the canopy ($x_0 = 35$ m) in the same vertical plane ($z_0 = 2.5$ m). The initial velocity of the brands is either zero or the local gas velocity. Many geometries of firebrands exist, which include cylinders and disks,

tensity, defined as the rate of energy release per unit time per unit length of fire front, and calculated by

representative of leaves, needles, and pieces of bark. As it was found that disks are carried the farthest and have the highest remaining mass fraction impacting the ground [18], disk-shaped firebrands with an initial aspect ratio, AR, ranging from 0.02 to 0.075 are considered here. The incidence angle of firebrands is equal to $\alpha_i = 145°$ for which the largest propagation is expected [14]. For the two fire intensities and the three wind speed conditions, a parametric study is carried out to assess the effect of varying the characteristics of firebrands: diameter (4, 6, 8, and 10 cm), thickness (2 and 3 mm), density (50, 100, and 150 kg m^{-3}) on their behavior. This means that for each fire intensity and wind speed, 24 firebrands are released. With a time step of 10^{-3} s, the calculation of transport and combustion of a firebrand does not exceed 20 s of CPU time.

3.2. Firebrand trajectories

Fig. 4 shows firebrand trajectories for a wind speed of 6.7 m s^{-1} in the symmetry plane and the horizontal planes $y = 8$ m and $y = 23$ m for the 10 and 40 MW m^{-1} fire intensities, respectively. Gas temperature contours and velocity vector fields are superimposed to provide a visualization of the fire plume.

Two regimes of motion can be observed: the first concerns firebrands that fall down near the canopy, whereas the second relates to particles that are lofted by the buoyant fire plume and land far away from the fire. For given flow conditions, the transition between the two regimes is mainly controlled by the product $\rho_f^{w0} \times \tau$. This is shown in Fig. 5, representing the distance traveled by firebrands as a function of this product. For small values of this product, the firebrands are lofted by the plume as the ratio between the gravitational and the aerodynamic forces which act on a brand is proportional to the product $\rho_f^{w0} \times \tau$. However, it can happen that, for the same flow conditions and the same values of the product $\rho_f^{w0} \times \tau$, only the heaviest firebrands (see for example firebrands A and B in Fig. 5) are entrained into the plume.

Let us now consider the firebrands that are transported by the plume. In the xy-plane, once released, the firebrand is uplifted by the strong buoyant flow. When the gravitational force prevails the aerodynamic forces, the brand starts to decrease its altitude and finally falls on the ground. It can be observed in Fig. 4 that the firebrands leave the plume when the gas temperature recovers the ambient value. In the xz-plane, the firebrands follow the streamlines of the gas flow. Near the canopy, they are dragged toward the symmetry plane due to air entrainment into the plume. As the firebrands are transported far from the canopy, they rise up and deviate from the symmetry plane due to convective structures. Four different histories of

flying embers are illustrated in Fig. 6, which show the time evolution of the mass and surface temperature of firebrands for a 10 MW m^{-1} fire and a wind speed of 15 mph. Firebrand (1) burns completely in flight after leaving the thermal plume, and firebrands (2) and (3) are glowing at landing, whereas firebrand (4) lands in a flaming state. Moreover, for values of α_f^{char} less than about 0.25, the firebrand can reach the ground with a low-level temperature. This scenario is not observed in the present study where one third of the heat released by char oxidation is assumed to be deposited at the particle surface. Unlike firebrands (1) to (3), firebrand (4), having the highest value of the product $\rho_f^{w0} \times \tau$, leaves early the fire plume and falls on the ground (e.g., see the trajectory of firebrands for $\tau = 3$ mm, $\rho_f^{w0} = 150$ kg m^{-3} in Fig. 4a). Although they do not cover a large distance upon landing, such firebrands are of particular interest since they have a high capability to ignite new spot fires. Manzello et al. [42] have shown experimentally that a single flaming firebrands ignite pine needle beds with a moisture up to 11% while a shower of glowing embers is required to produce potential ignitions.

Let us consider the mass and surface temperature of the firebrand (1) in Fig. 6. During the first 42 s of flight when the firebrand is pyrolyzing, a small amount of oxygen diffuses towards the solid surface, which limits char oxidation. At the end of pyrolysis, the remaining dimensionless mass is then very close to $\nu_f^{char} = 0.39$. This means that we can assume that pyrolysis and char oxidation processes occur successively. After 42 s, and for a few seconds, radiative and convective losses cause the surface temperature to decrease sharply. Then, the heat produced by the heterogeneous combustion balances heat losses to slow down the decrease in surface temperature. An equilibrium temperature of about 475 K is reached at $t = 92$ s. As the diameter decreases, the charring reaction rate R_f^{char} is enhanced. This explained the subsequent rise in temperature. Firebrands (2) and (3) do not exhibit such behavior. The increase in heat production by char oxidation due to the reduction in diameter cannot compensate losses, which explains why the temperature is always decreasing.

Model results show that, for the firebrands considered, the pyrolysis occurs in the thermally thin heat transfer regime, which indicates that the pyrolysis time is proportional to the product $\rho_f^{w0} \times \tau$. This explains why pyrolysis process of firebrands (1) and (2) follow the same trends, whereas that of firebrand (3) is about twice as long. Concerning char oxidation of firebrands (1)–(3) in Fig. 6, the difference in the time evolution of the mass can be explained from the following analysis. As Reynolds numbers encountered are relatively large (>300), Eq. (23) reduces to
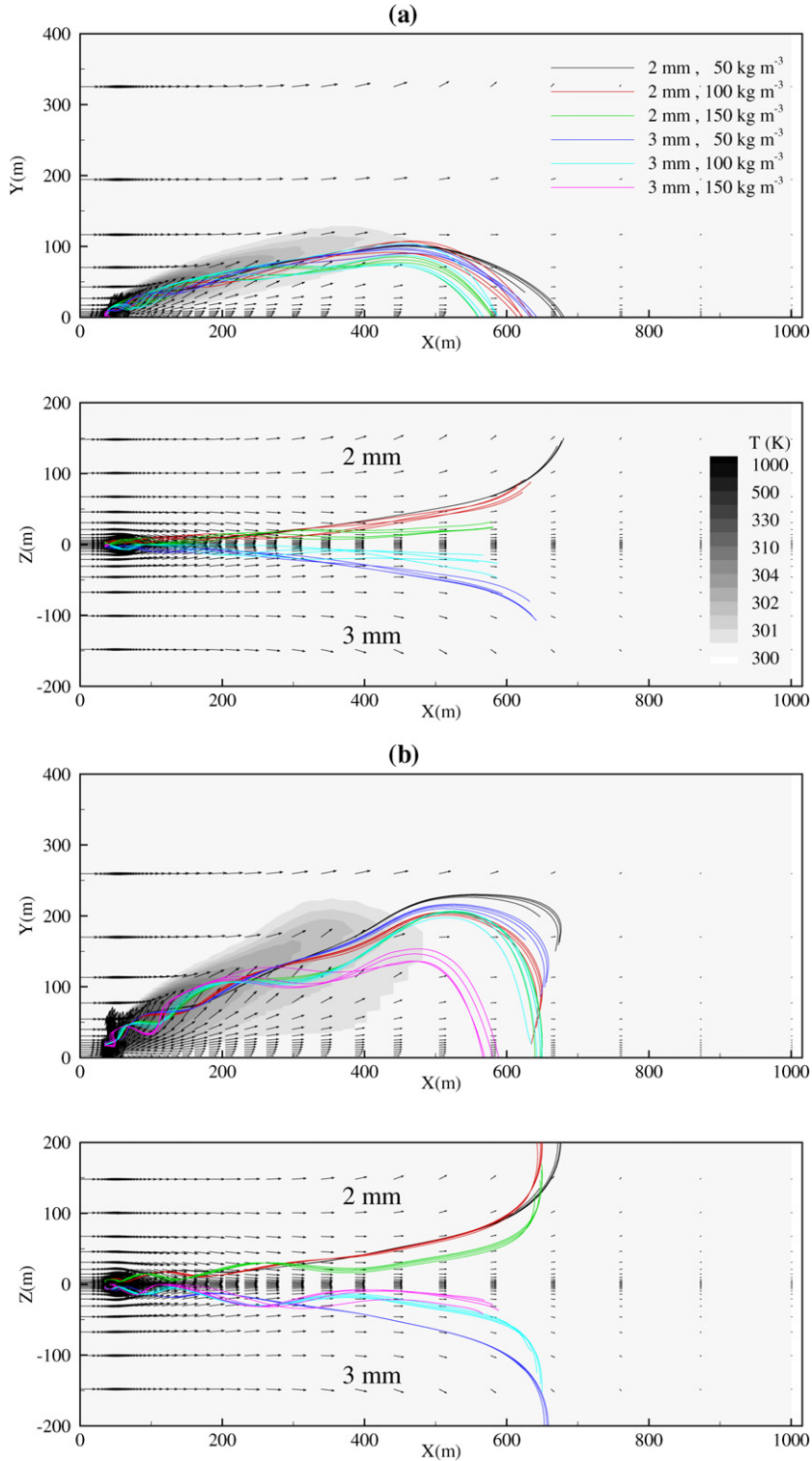
Fig. 4. Firebrand trajectories projected in the planes $z = 0$ m and $y = 8$ m for the 10 MW m^{-1} fire (a) and $z = 0$ m and $y = 23$ m for the 40 MW m^{-1} fire (b). Trajectories of firebrands launched from the top of the canopy are superimposed on steady-state gas temperature contours and velocity vector fields. Wind speed is 15 mph. The initial velocity of the firebrands is equal to the local gas velocity. Lines of the same color correspond to particles with the same thickness and density but different diameter.
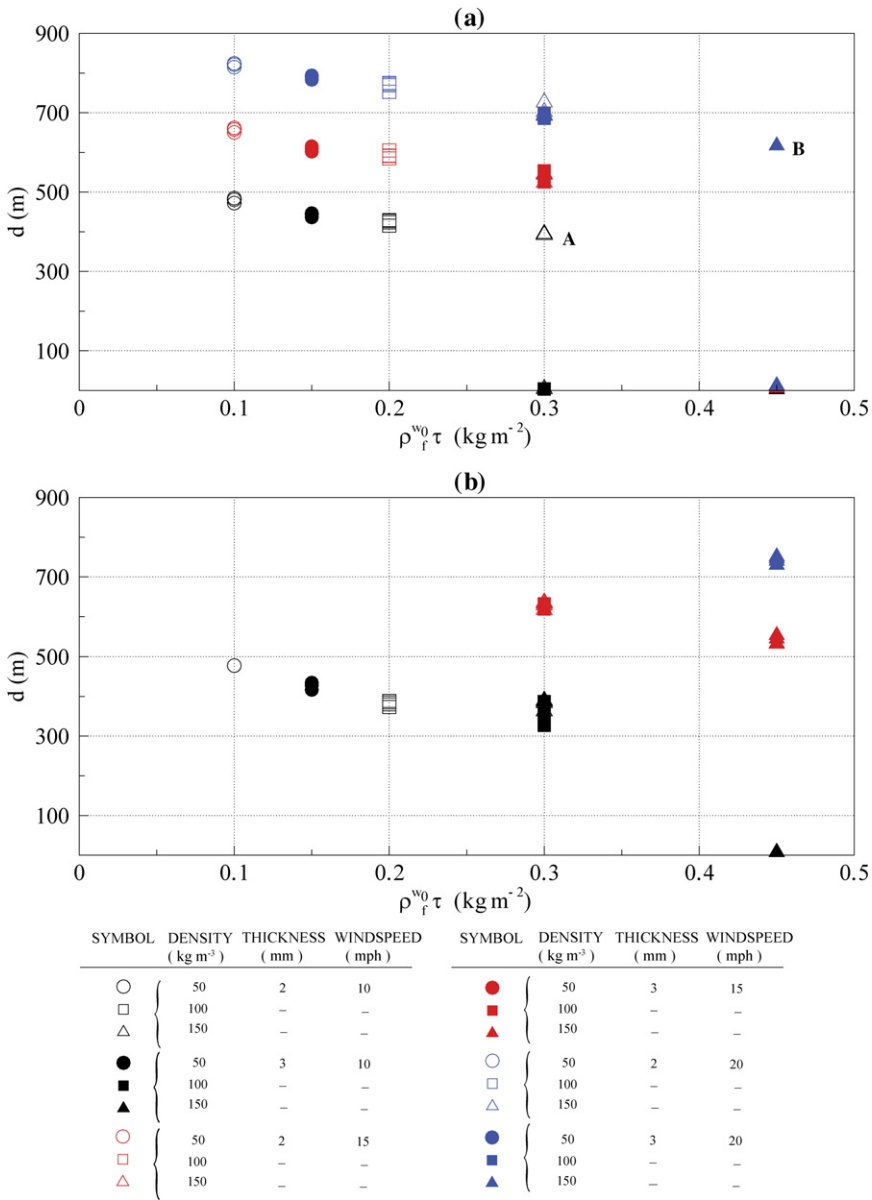
Fig. 5. Landing distance d versus the product $\rho_{\mathrm{f}}^{w_0} \times \tau$ for the 10 MW m^{-1} fire (a) and the 40 MW m^{-1} fire (b). The three wind speeds 10, 15, and 20 mph are considered. The initial velocity of the firebrands is equal to the local gas velocity.

$$\frac{\pi}{4}\tau\rho_{\mathrm{f}}^{\mathrm{char}}\frac{\mathrm{d}D^2}{\mathrm{d}t} \simeq 0.272 \mathrm{Sc}^{1/3}\,\mathrm{Re}^{1/2}\,R_{\mathrm{f}}^{\prime\,\mathrm{char}}S_{\mathrm{ox}}. \quad (32)$$

The characteristic time for char oxidation can be deduced from the above equation using $\rho_{\mathrm{f}}^{\mathrm{char}} = v_{\mathrm{f}}^{\mathrm{char}}\rho_{\mathrm{f}}^{w_0}$, $\mathrm{Re} = (\frac{3}{2}D^2\tau)^{1/3}\rho_{\mathrm{film}}\|\mathbf{V}_{\mathrm{rel}}\|/\mu_{\mathrm{film}}$, and assuming that the product $R_{\mathrm{f}}^{\prime\,\mathrm{char}}S_{\mathrm{ox}}\|\mathbf{V}_{\mathrm{rel}}\|^{1/2}$ is independent of time during the char oxidation process. Fig. 7 shows that this assumption can be reasonably made. It is then found that the characteristic time for total char oxidation scales with $\rho_{\mathrm{f}}^{w_0}D_0^{5/3}$.

A fitting of model results, given in Fig. 8, shows exponential behavior of the remaining mass with a normalized flight time for firebrands that land in a flaming state,

$$M_{\mathrm{final}}/M_0 = 0.9727e^{-0.0047x}, \quad (33)$$

with $x = t_{\mathrm{flight}}/(\rho_{\mathrm{f}}^{w_0}\tau)$, whereas it exhibits linear behavior for firebrands glowing at landing,

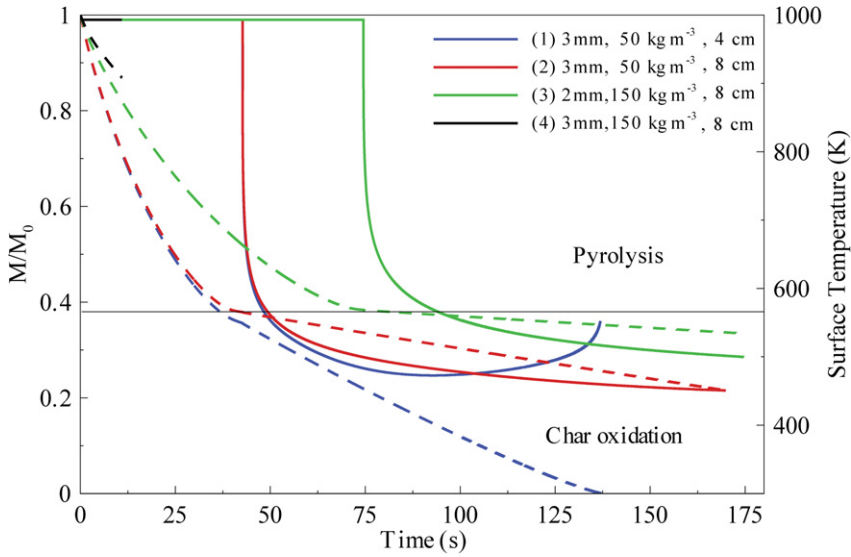$$M_{\mathrm{final}}/M_0 = -0.0007x + 0.3864, \quad (34)$$

Fig. 6. Time evolution of the mass fraction (dashed lines) and surface temperature (solid lines) of four firebrands launched from the top of the canopy. Fire intensity is 10 MW m^{-1} and wind speed is 15 mph. The initial velocity of the firebrands is equal to the local gas velocity.

Fig. 7. Time evolution of the expression $R_f'^{char} S_{ox} \|\mathbf{V}_{rel}\|^{1/2}$ of two firebrands launched from the top of the canopy. Fire intensity is 10 MW m^{-1} and wind speed is 10 mph. The initial velocity of the firebrands is equal to the local gas velocity.
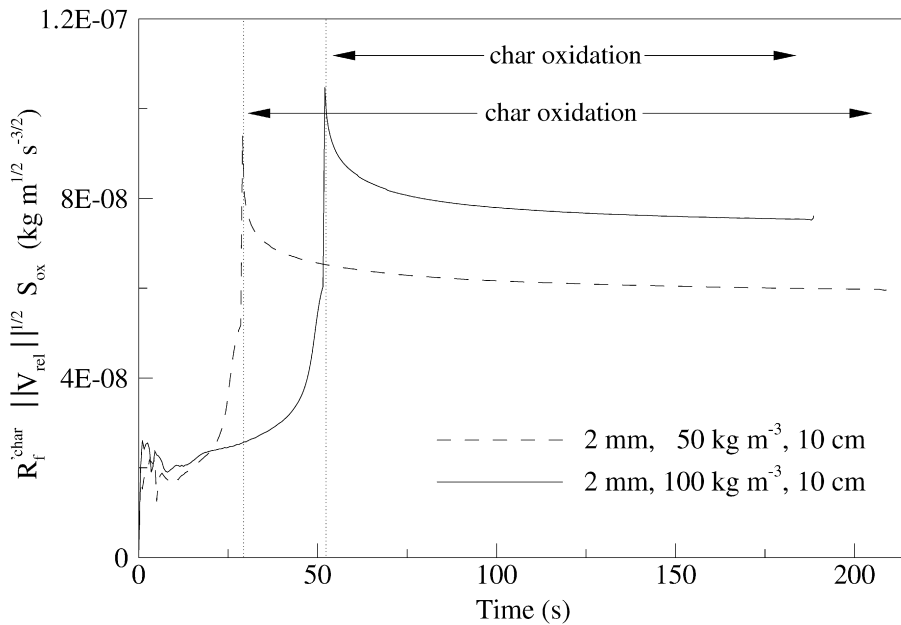
with $x = t_{flight}/(\rho_f^{w0} D_0^{5/3})$.

3.3. Landing distance and lofted firebrand height

Fig. 5 shows the landing distance of different firebrands vs the product $\rho_f^{w0} \times \tau$ for the various fire intensities and wind speeds. Firebrands differ in thickness, diameter, and density. Results show that the landing distance decreases as the product $\rho_f^{w0} \times \tau$, which characterizes the ratio between the gravitational and the aerodynamic forces which act on a brand, increases.

It can also be observed that d increases almost linearly with wind speed as a result of the increase
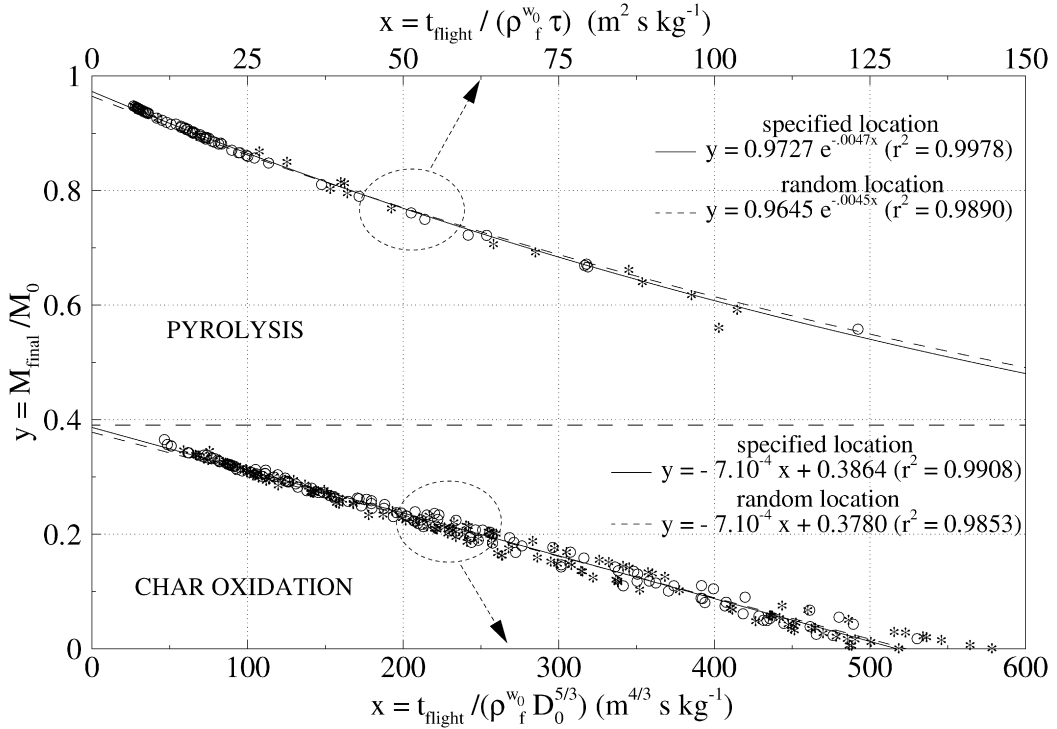
Fig. 8. Remaining mass fraction versus the flight time normalized by the product $\rho_f^{w0} \times \tau$ for flaming firebrands at landing (top part) or by the product $\rho_f^{w0} \times D_0^{5/3}$ for glowing firebrands at landing (bottom part). Circles correspond to firebrands initially launched from a specified location, at the top of the canopy. Stars refer to firebrands initially released from randomly generated locations within the canopy. The initial velocity of the firebrands is equal to the local gas velocity.

in the flying distance inside the plume. The landing distance is not sensitive to the initial diameter of the disk-shaped firebrands, in accordance with Anthenien et al. [18] and Himoto and Tanaka [43], and is weakly dependent on the fire intensity as a result of buoyancy effects.

A power-law fit of the data describes the dependence of d on these parameters (see Fig. 9)

$$d \propto I^{0.1} U_{\text{wind}}^{0.9} \left(\rho_f^{w0} \times \tau \right)^{-0.2}. \qquad (35)$$

Note that the range of validity of the power-law has been extended by randomly varying the product $\rho_f^{w0} \times \tau$ in the range 0.03–0.8. This corresponds to about 1000 firebrands launched from burning trees.

It can be observed that the landing distance is not sensitive to the initial velocity of firebrands (Figs. 9a and 9b), as the brand velocity rapidly becomes close to that of the gas.

The role of fire intensity on the maximum height of lofted firebrands, h_{max}, is shown in Fig. 10. As expected, for most firebrands, the higher the fire intensity, the greater the maximum height, with an enhanced influence of wind for the 40 MW m^{-1} fire. Although the maximum height is smaller for fires of low intensity, this does not lead to significantly

smaller landing distances due to more straight trajectories (Fig. 4).

3.4. Effect of the initial placement of firebrands

In order to show how initial placement affects firebrand behavior, 1000 disk-shaped firebrands are now released from randomly-generated locations within the canopy. Model results concerning the remaining mass fraction and landing distance are plotted in Figs. 8 and 9 for the different fire intensities, wind speeds and firebrand properties. The very small departure from the fitting curves shows that Eqs. (33)–(35) remain valid, whatever the initial placement of firebrands.

4. Conclusion

A numerical model has been developed to gain better understanding of the transport and combustion of firebrands responsible for spot wildland fire spread. A parametric study is performed to determine the effect of the fire intensity, wind conditions, and firebrand properties on firebrand behavior. A special
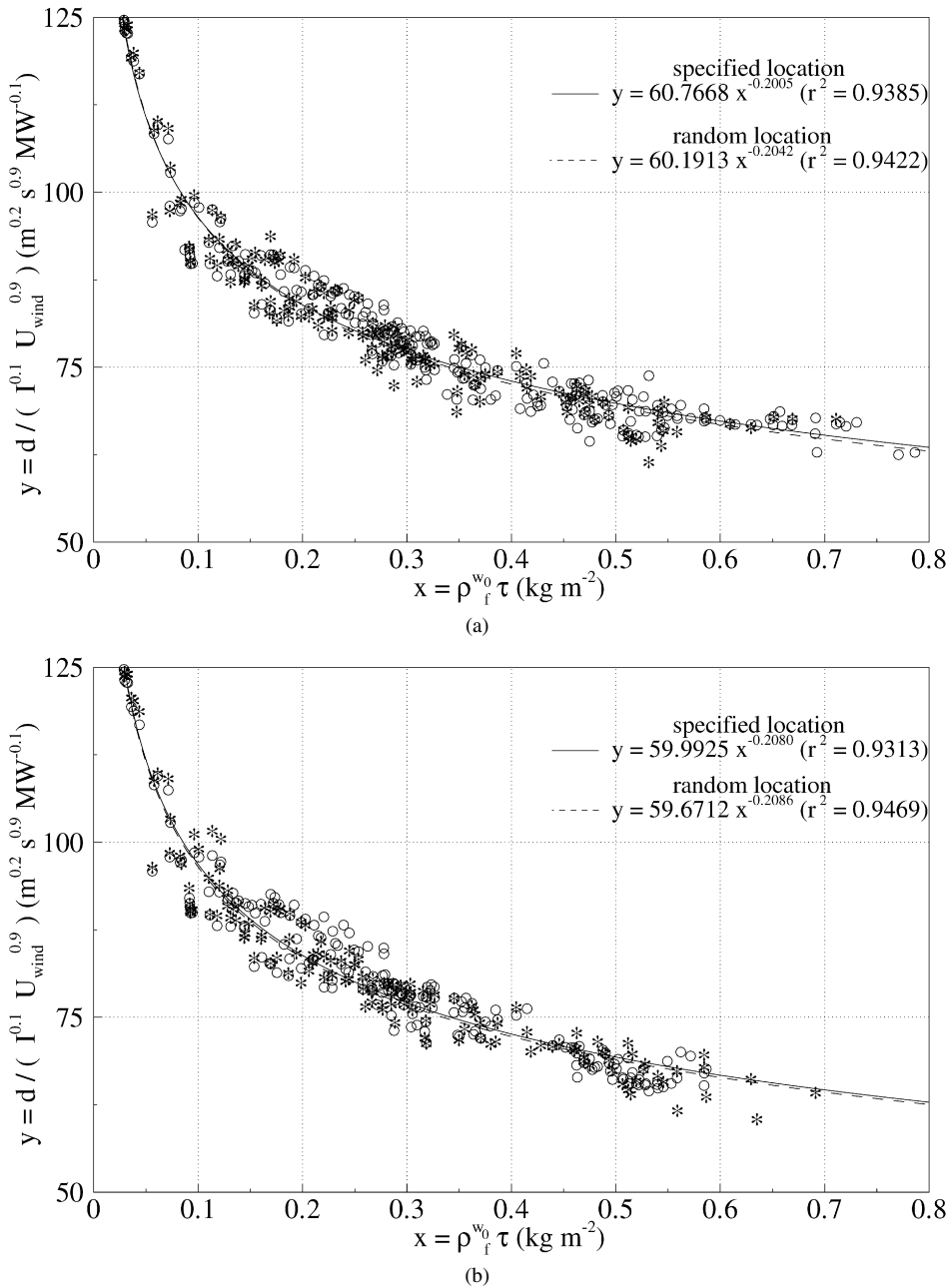
(a)

(b)

Fig. 9. Landing distance d, normalized by $I^{0.1} U_{\text{wind}}^{0.9}$, versus the product $\rho_f^{w_0} \times \tau$ for glowing firebrands at landing, those which fall on the ground far from the fire front. Brands are launched with an initial velocity equal to the gas phase velocity (a) and to a zero-value velocity (b). Circles correspond to firebrands initially launched from a specified location, at the top of the canopy. Stars refer to firebrands initially released from randomly generated locations within the canopy.

emphasis has been put on the combustion model of the firebrands since their burning diameter at landing determines the potential for the firebrand to ignite the adjacent vegetation.

It is found that the distance reached by the firebrand varies almost linearly with wind speed, while it depends very weakly on fire intensity. This distance is

shown to be independent of the initial particle diameter and to follow a decreasing power-law function of the product $\rho_f^{w_0} \times \tau$. For firebrands in flaming state at landing, their mass is found to be an exponential decay of the flight time normalized by the product $\rho_f^{w_0} \times \tau$. For embers that remain aloft for a long period of time, there is a linear relationship between
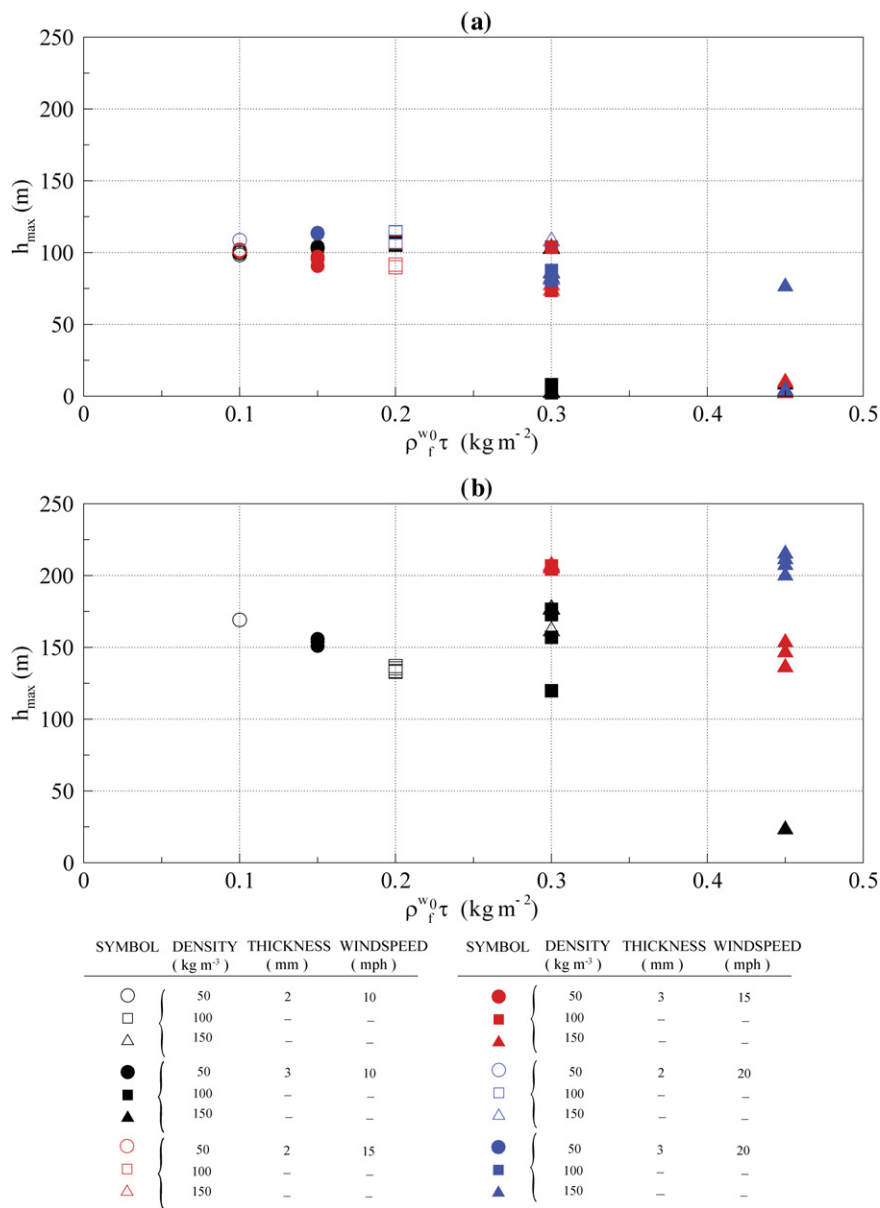
(a)

(b)

SYMBOL	DENSITY (kg m⁻³)	THICKNESS (mm)	WINDSPEED (mph)	SYMBOL	DENSITY (kg m⁻³)	THICKNESS (mm)	WINDSPEED (mph)
○	50	2	10	●	50	3	15
□	100	–	–	■	100	–	–
△	150	–	–	▲	150	–	–
●	50	3	10	○	50	2	20
■	100	–	–	□	100	–	–
▲	150	–	–	△	150	–	–
○	50	2	15	●	50	3	20
□	100	–	–	■	100	–	–
△	150	–	–	▲	150	–	–

Fig. 10. Lofted firebrand maximum height versus the product $\rho_f^{w0} \times \tau$ for the 10 MW m^{-1} fire (a) and the 40 MW m^{-1} fire (b). The three wind speeds 10, 15, and 20 mph are considered. The initial velocity of the firebrands is equal to the local gas velocity.

their mass at landing and the flight time normalized by $\rho_f^{w0} D_0^{5/3}$. These relationships are found to be independent of the initial firebrand placement.

References

[1] C.S. Tarifa, P.P. Del Notario, F.G. Moreno, Proc. Combust. Inst. 10 (1965) 1021–1037.

[2] C.S. Tarifa, P.P. Del Notario, F.G. Moreno, A.R. Villa, Transport and Combustion of Firebrands, Reports of GRANTS FG-SP-114 and FG-SP-146, U.S. Dept. of Agriculture Forest Service, 1967.

[3] S.L. Lee, J.M. Hellman, Combust. Flame 13 (1969) 645–655.

[4] S.L. Lee, J.M. Hellman, Combust. Flame 15 (1970) 265–274.

[5] A. Muraszew, J.B. Fedele, W.C. Kuby, Combust. Flame 30 (1977) 321–324.

[6] A. Muraszew, J.B. Fedele, W.C. Kuby, Firebrand Investigation, Aerospace Report ATR-75 7470-1, The Aerospace Corp., 1975.

[7] F.A. Albini, Spot Fire Distance from Burning Trees—A Predictive Model, USDA Forest Service Research Paper INT-56, Intermountain Forest and Range Experiment Station, 1979.

[8] F.A. Albini, Spot Fire Distance from Isolated Sources—Extensions of a Predictive Model, USDA Forest Service Research Paper INT-309, Intermountain Forest and Range Experiment Station, 1981.

[9] F.A. Albini, Potential Spotting Distance from Wind-Driven Surface Fires, USDA Forest Service Research Paper INT-309, Intermountain Forest and Range Experiment Station, 1983.

[10] F.A. Albini, Combust. Sci. Technol. 32 (1983) 277–288.

[11] J.P. Woycheese, P.J. Pagni, in: Proceedings of the Annual Conference on Fire Research (NISTIR 5904), Gaithersburg, MD, 1996, p. 67.

[12] J.P. Woycheese, P.J. Pagni, in: Proceedings of the 2nd International Conference on Fire Research and Engineering, Society of Fire Protection Engineers, Washington, USA, 1998, p. 137.

[13] J.P. Woycheese, P.J. Pagni, D. Liepmann, J. Fire Protect. Eng. 10 (1999) 32–44.

[14] J.P. Woycheese, P.J. Pagni, in: Proceedings of the 3rd International Conference on Fire Research and Engineering, Society of Fire Protection Engineers, Washington, USA, 1999, p. 53.

[15] P.J. Pagni, J.P. Woycheese, Proceedings of the 15th Joint Panel Meeting on Fire Research and Safety, U.S./Japan Government Cooperative Program on Natural Resource (UJNR), San Antonio, USA, 2000, p. 373.

[16] J.P. Woycheese, in: Proceedings of the 9th International Interflam Conference, Interscience Communications Ltd., Edinburgh, Scotland, 2001, p. 101.

[17] S.D. Tse, A.C. Fernandez-Pello, Fire Safe. J. 30 (1998) 333–356.

[18] R.A. Anthenien, S.D. Tse, A.C. Fernandez-Pello, Fire Safe. J. 41 (2006) 349–363.

[19] P.F. Ellis, The Aerodynamic and Combustion Characteristics of Eucalypt Bark—A Firebrand Study, Ph.D. dissertation, Department of Forestry Australian National University, 2000.

[20] M.R. Raupach, Math. Comput. Model. 13 (12) (1990) 113–121.

[21] B. Porterie, D. Morvan, J.C. Loraud, M. Larini, Phys. Fluids 12 (2000) 1762–1782.

[22] B. Porterie, S. Nicolas, J.L. Consalvi, J.C. Loraud, F. Giroud, C. Picard, Numer. Heat Trans. Part A 47 (2005) 571–591.

[23] R.J. Kee, F.M. Rupley, J.A. Miller, CHEMKIN-II: A Fortran Chemical Kinetics Package for the Analysis of Gas Phase Chemical Kinetics, Report No. SAND89-8009B, Sandia National Laboratories, 1993.

[24] D. Sucker, H. Brauer, Wärme Stoffübertragung 8 (1975) 149–158.

[25] H. Kramers, Physica 12 (1946) 61–80.

[26] A.M. Grishin, Mathematical Modeling of Forest Fires and New Methods of Fighting Them, Pub. House of the Tomsk University, Tomsk, 1997.

[27] B.F. Magnussen, B.H. Hjertager, Proc. Combust. Inst. 16 (1976) 719–729.

[28] J.L. Consalvi, B. Porterie, J.C. Loraud, Int. J. Heat Mass Transfer 45 (2002) 2755–2768.

[29] C.R. Kaplan, C.R. Shaddix, K.C. Smyth, Combust. Flame 106 (1996) 392–398.

[30] B.P. Leonard, J.E. Drummond, Int. J. Numer. Methods Eng. 20 (1995) 421–442.

[31] W.K. Chow, Y.L. Cheung, Numer. Heat Trans. Part A 31 (1997) 87–112.

[32] S.V. Patankar, Numerical Heat Transfer and Fluid Flow, McGraw–Hill, New York, 1980.

[33] G.D. Raithby, E.H. Chui, J. Heat Transfer 112 (1990) 415–423.

[34] C. Yin, L. Rosendahl, S.K. Kaer, H. Sorensen, Chem. Eng. Sci. 58 (2003) 3489–3598.

[35] C. Lindenburg, in: Proceedings of the IEA Symposium on the Aerodynamics of Wind Turbines, ECN-RX-01-004, NREL, USA, 2000.

[36] M.F.R. Mulcahy, I.W. Smith, Rev. Pure Appl. Chem. 19 (1969) 81–100.

[37] N. Frössling, Gerlands Beitr. Geophys. 52 (1938) 170–216.

[38] K.M. Bryden, K.W. Ragland, C.J. Rutland, Biomass Bioenergy 22 (2002) 41–53.

[39] C. Di Blasi, Combust. Flame 97 (1994) 225–239.

[40] H. Panofsky, J. Dutton, Atmospheric Turbulence, Wiley, New York, 1984.

[41] G.M. Byram, in: K.P. Davis (Ed.), Combustion of Forest Fuels, McGraw–Hill, New York, 1959, p. 61.

[42] S.L. Manzello, T.G. Cleary, J.R. Shields, J.C. Yang, in: Proceedings of 4th Joint Meeting of the U.S. Sections of the Combustion Institute, The Combustion Institute, Philadelphia, USA, 2005, pp. 1–6.

[43] K. Himoto, T. Tanaka, in: Proceedings of the 8th International Symposium on Fire Safety Science, Beijing, China, 2005, p. 433.